High Sensitivity Core-Shell Structure (CSS)-Based Fiber Sensor for Monitoring Analytes in Liquids and Gases

Tianyu Yang, Can Ding, *Member, IEEE,* Richard W. Ziolkowski, *Life Fellow, IEEE* and Y. Jay Guo, *Fellow, IEEE,*

***Abstract*—A compact and robust mid-infrared refractive index-based microstructured fiber sensor with high sensitivity is developed for monitoring analytes in liquids and gases. Resonant core-shell elements facilitate its exceptional performance. The theory underpinning them is explained, and the evolution of the fiber structure is presented. The material choices and details of the microstructure leading to its optimization are described. Simulation results demonstrate that the optimized fiber sensor can readily detect refractive index variations in the range from 1.0 to 1.41 and that its wavelength sensitivities are 2510 and 4303 nm/RIU for analyte detection, respectively, in gases and liquids. It is an excellent candidate for environmental monitoring applications.**

***Index Terms*—terahertz, fiber characteristic, single-polarization singel-mode.**

I. Introduction

OPTICAL fiber technologies have been used in sensor applications for over 30 years. They have many benefits including noncontact measurement and immunity to electromagnetic interference, which makes them very suitable for sensor designs [1]. Moreover, fiber optics offers an ability to work over very long distances in some circumstances, e.g., a fiber sensor can be kilometers away from the monitoring area. The use of microstructure fibers for sensing applications has attracted serious attention and efforts in the last decade. Various physical mechanisms have been used in fiber sensing applications. Examples include exploiting Mach-Zehnder interference [2], Fabry-Perot resonance [3], enhanced Raman scattering [4], fiber loop mirror [5], and plasmonic resonances [6] to detect various physical or chemical parameters. Consequently, diverse fiber-based sensors have been experimentally and theoretical demonstrated for the sensing variations of temperature [7], humidity [8], strain [9], pH [10], electric and magnetic fields [11], [12], and permittivity (or refractive index) [13].

The permittivity or refractive index is a fundamental physical property of every medium which can be used to ascertain the true nature of a substance and determine the concentrations of its presence in various environments. Refractive index optical fiber based sensors are proven devices for prompt and label-free applications, such as measuring gas or liquid concentrations and characterizing biological interactions [14]. In particular, these devices have been adopted for measuring the refractive index changes of bio-analytes, e.g., deoxyribonucleic (DNA), ribonucleic acid (RNA), proteins, and viruses [15], [16]. A liquid-filled D-shaped fiber was proposed in [7] to serve as an in-fiber Mach-Zehnder (MZ) interferometer. By measuring the refractive index variations caused by temperature changes, optical fiber sensors have been employed for temperature sensing with a sensitivity of -84.72 nm/RIU. A compact MZ interferometer for refractive index sensing based on a tapered photonic crystal fiber (PCF) was developed in [2]. The sensor had a refractive index sensitivity of 51.9 nm/RIU and detected refractive index variations ranging from 1.3411 to 1.3737. Ref [17] reported a lossy mode resonance based tapered-tip optical fiber sensor that was coated with aluminium doped zinc oxide (AZO) and titanium oxide layers. The sensitivity of the reported sensor was above 1500 nm/RIU over a refractive index range from 1.33 to 1.45. A refractive index based sensor was developed in [18] on a PCF platform in the mid-infrared (mid-IR) region. Its detection range was from 1.23 to 1.29 with a high sensitivity, 5500 nm/RIU. Note that although aforementioned works attained high sensitivities, they focused on assessing liquid analytes and the refractive index detection range was small.

In comparison to liquid sensors, it is much harder for gas sensors to measure refractive index changes in the detection range from 1.0 to 1.1 with a high sensitivity. For instance, a Fano resonance based refractive index sensor was developed in [19] that attained the sensitivity and sensitivity per linewidth of 596 nm/RIU and 7.5, respectively, only from 1 to 1.05. On the other hand, a mid-IR photonic crystal waveguide based refractive index sensor was reported in [20] that achieved an average sensitivity of only 390 nm/RIU and a sensitivity per linewidth of only 4.5 from 1.0 to 1.1. It has been found to be very difficult to achieve sensitivities greater than 1000 nm/RIU which are in demand for gas sensors since the refractive index variation is quite small when the analyte in the gas changes.

A SiC-loaded single-polarization single-mode (SPSM) PCF was reported recently in [21]. When designing the SPSM PCF in the long-wavelength infrared (LWIR), an unexpected resonance was observed. The resonance wavelength was sensitive to the permittivity of the material flowing through the air holes of the PCF. The PCF was thus considered for a LWIR sensor.

This work was supported by the Australian Research Council (ARC) DECRA grant number DE200101347.

T. Yang, C. Ding, R. W. Ziolkowski, and Y. J. Guo are with the Global Big Data Technologies Centre, University of Technology Sydney, Ultimo, NSW 2007, Australia.

T. Yang is also with Opto-Electronic Engineering and Technology, Shenzhen Institute of Advanced Technology, Chinese Academy of Sciences, Shenzhen 518055, China.

Corresponding author: Can Ding, can.ding.1989@gmail.com.

Moreover, it was found that the resonance is mainly caused by the core-shell structures (CSSs) implemented in the cladding of the PCF. A core-shell theory [22], [23] was developed to provide insights into this resonance phenomenon. Although the realized sensitivity of the reported PCF-based spectrometer was only moderate, i.e., 566.6 nm/RIU, the concept was found to have a high potential to achieve higher sensitivity for sensing analytes in gases and liquids at mid-IR wavelengths.

In this work, the core-shell theory is further developed in Section II to maximize its potential to achieve a high sensitivity. The details and its application to correctly choose the plasmonic material are discussed in Section III and to optimize the structured fiber-based sensor configuration are presented in Section IV. While the CSSs, i.e., the SiC-loaded air holes in the PCF, provided the resonant absorption mechanism in the previous work [21], it will be demonstrated that the PCF itself is not necessary to achieve the resonance. The evolution of the fiber design in this work begins with an idealized cylindrical CSS surrounded by a substrate-based cylindrical wall, i.e., an idealized suspended core-shell structured fiber. It is shown that the response of such a fiber is very sensitive to any gas or liquid analyte that flows through its air regions. Several modifications of the initial fiber are described that maximize its sensing performance and make it a feasible suspended-core design in practice. Simulation results will demonstrate that the resultant CSS-based fiber sensor can readily detect refractive index variations in the range from 1.0 to 1.41 and that its wavelength sensitivities are 2510 and 4303 nm/RIU for gas and liquid analyte detection, respectively. Moreover, comparisons with previously reported mid-IR refractive index-based sensors demonstrate that this innovative fiber-based sensor has a much higher sensitivity and enhanced figure of merit.

II. Resonant Core-Shell Structure (CSS) Fundamentals

As shown in Fig. 1, the basic geometry of the core-shell structure (CSS) considered here is a three-region cylindrical configuration. The Regions 1 to 3 are taken to be filled, respectively, with air, a dispersive plasmonic material, and substrate with relatively flat frequency dispersion. The corresponding relative permittivity of each region is ε_1, ε_2, and ε_3, respectively. In order for the plasmonic resonance of the *m*-th multipole mode in this core-shell geometry to be excited, the ratio of the two radii, ρ_1 and ρ_2, needs to satisfy the relation [21]:

$$\frac{\rho_1}{\rho_2} = \sqrt[2m]{\frac{[\varepsilon_2(\omega)+\varepsilon_1][\varepsilon_2(\omega)+\varepsilon_3]}{[\varepsilon_2(\omega)-\varepsilon_1][\varepsilon_2(\omega)-\varepsilon_3]}}. \quad (1)$$

Since the material in Region 2 is dispersive, ε_2 is a function of the excitation frequency.

Assume that the values of ρ_1/ρ_2, ε_1, and ε_3 are fixed and that those permittivities are non-negative. The specific values of ε_2 that satisfy Eq. 1 for the *m*-th multipole mode are then readily determined. Once these values have been calculated, the corresponding resonance wavelengths are simply obtained from the dispersion properties of the material. Let

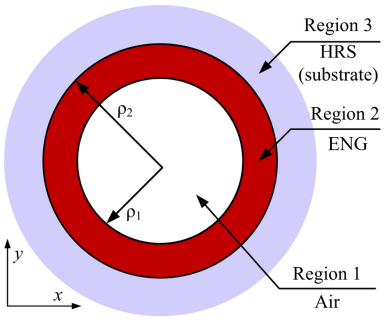

Fig. 1. Cylindrical core-shell structure (CSS) geometry.

$$\left(\frac{\rho_1}{\rho_2}\right)^{2m} = A, \quad (2)$$

Eq. 1 then becomes

$$(A-1)\varepsilon_2{}^2 - (A+1)(\varepsilon_1+\varepsilon_3)\varepsilon_2 + (A-1)\varepsilon_1\varepsilon_3 = 0. \quad (3)$$

This is a quadratic equation with one unknown, ε_2. It has the two well-known solutions:

$$\varepsilon_2 = \frac{-b \pm \sqrt{b^2-4ac}}{2a}, \quad (4)$$

where

$$a = A-1, \quad b = -(A+1)(\varepsilon_1+\varepsilon_3), \quad c = (A-1)\varepsilon_1\varepsilon_3. \quad (5)$$

Plasmonic modes will occur if the ENG layer is very thin, i.e., if the ratio ρ_1/ρ_2 is close to 1. Thus, they will occur if one takes *A* very close to 1 so that $a \approx 0$ and $4ac \approx 0$. The two solutions of ε_2 are then

$$\varepsilon_2 = 0 \text{ or } \frac{A+1}{A-1}\cdot(\varepsilon_1+\varepsilon_3). \quad (6)$$

This means that Region 2 is either an epsilon-zero (EZ) medium or an epsilon-negative (ENG) medium with $|\varepsilon_2| >> 1$ because $A = \rho_1/\rho_2$ must be close to, but less than one.

Now consider the case where the values of ε_1 in the cylindrical CSS are changed by allowing a gas or liquid to flow through Region 1. Different values of ε_2 will then be necessary to satisfy the resonance condition (6). Consequently, the resonance will occur at a different wavelength, i.e., at a wavelength that depends on the material in Region 1. Moreover, it is clear from (6) that because of the large coefficient $(A+1)/(A-1)$, the ENG solution of ε_2 is much more sensitive to a variation in ε_1 than the EZ one is. Thus, it is the one more suited for sensing purposes.

By properly exciting the plasmonic modes in the CSS and properly measuring the wavelength shift of the resonance, one can determine the change in the relative permittivity and, hence, the refractive index of Region 1. The sensitivity, *S*, is thus calculated by the derivative of the resonance wavelength with respect to the real part of the permittivity of Region 1, $Re(\varepsilon_1)$, which by the chain-rule means

$$S = \frac{d(\lambda)}{d(Re(\varepsilon_1))} = \frac{d(\lambda)}{d(Re(\varepsilon_2))} \times \frac{d(Re(\varepsilon_2))}{d(Re(\varepsilon_1))}. \quad (7)$$

The first term of the product in Eq. 7 is determined from the material dispersion characteristics of the material in Region 2. It will be denoted as B_2. The second term of the product can be obtained from Eq. 6. Therefore, the sensitivity can be simplified to the expression:

$$S = B_2 \times \frac{d(Re(\varepsilon_2))}{d(Re(\varepsilon_1))} = B_2 \times \frac{A+1}{A-1}. \quad (8)$$

This result yields two conclusions. The first is that the sensitivity increases with the magnitude of B_2. This outcome helps one determine which dispersive material would be preferred to achieve a high sensitivity. This detail will be discussed further in Section III. The second one is that the overall sensitivity will be higher when A is as close to 1 as possible. This outcome tells us that when a sensor design is based on the CSS, the thickness of Region 2 needs to be as small as possible.

III. Material Selection

The core-shell resonance theory is used to determine what kind of material (in terms of relative permittivity) is needed in Region 2 to achieve a very high sensitivity. Fundamentally, as shown above, the permittivity of Region 2 must be dispersive. Moreover, it must have a negative real part, i.e., it must be a plasmonic material or the resonance would not exist. Furthermore, it was found that B_2, i.e., the variation of the wavelength with respect to $Re(\varepsilon_2)$ needs to be large. This means that the material dispersion curve with respect to wavelength should be as flat as possible.

To illustrate this fact more intuitively, we use two different example ENG materials to illustrate the relationship between the material dispersion and the resulting sensitivity. As shown in Fig. 2, the real part of the permittivity of Material 1 is defined to have a smaller slope than that of Material 2. We allow the permittivity of whatever material is in Region 1 to vary in the range from 1.0 to 1.1. The value of the real part of the permittivity in Region 2 then needs to change from -1.0 to -2.0 in order for the resonance condition to be satisfied. As illustrated in Fig. 2, the resonance wavelength shift in the case that Region 2 is filled with Material 1 is Shift 1 ($\sim$ 0.5 μm). When Region 2 is filled with Material 2, the wavelength shift is Shift 2 ($\sim$ 0.25 μm). Since (8) indicates that a larger wavelength shift is indicative of a higher sensitivity, it is thus concluded that a material in Region 2 with the flattest dispersion curve will yield the highest sensitivity.

Since the material in Region 2 must be an ENG medium, it must be lossy. Numerous simulation results have shown that a smaller imaginary part of the relative permittivity, i.e., $Im(\varepsilon_2)$, is preferred for the desired sensor application. A larger $Im(\varepsilon_2)$ means a higher loss in Region 2, which in turn leads to a detuning of the resonance, i.e., a decrease in its peak response and a broadening of its width. Thus a large loss ENG material would make it much harder to detect the resonance peak in a practical system.

Among the different kinds of plasmonic materials in the optical regime, conductive metal oxides (CMO) have recently attracted much attention as plasmonic ENG materials. This is due to their advantageous properties at near- and mid-IR wavelengths, e.g., their tuneable carrier densities and lower material losses, especially when compared to noble metals [24]. Among recently reported CMOs, e.g., aluminium-doped zinc oxide (AZO), gallium-doped zinc oxide (GZO), indium-tin-oxide (ITO) [24], [25], and dysprosium-doped cadmium oxide (CdO) [26], AZO and CdO have low loss factors. Thus, they serve currently as the best candidates for the intended CSS-based fiber sensor design.

Fig. 3(a) plots for comparison the real and imaginary parts of the relative permittivity of AZO and CdO. It is observed that

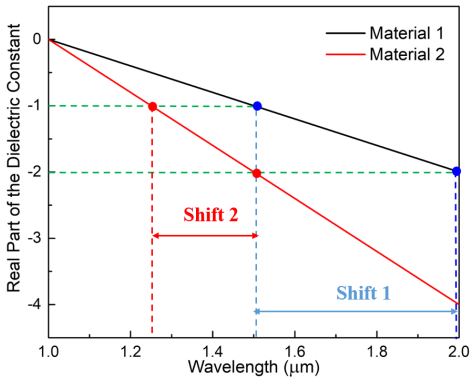

Fig. 2. Illustration of the difference of the resonance wavelength shift when Region 2 of the CSS is filled with different materials.

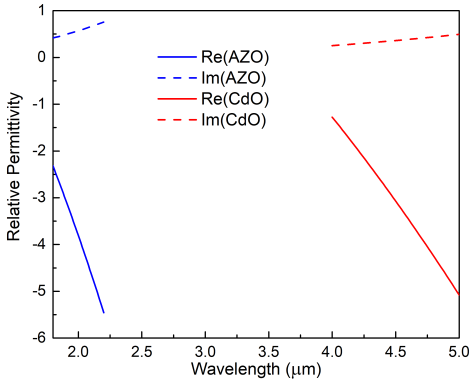

(a)

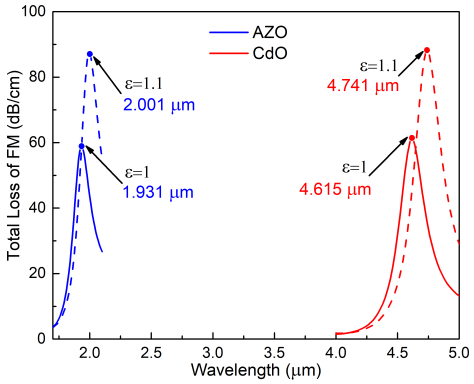

(b)

Fig. 3. Study of the sensitivity of the suspended CSS-based fiber sensor to the choice of the ENG material in Region 2. (a) Real and imaginary parts of the relative permittivity of AZO and CdO. (b) The total loss of the fundamental propagating mode of the CSS-based suspended fiber filled with AZO and CdO.

TABLE I
COMPARISON OF THE SENSING PERFORMANCE OF THE SUSPENDED CSS-BASED FIBER SENSOR WITH AZO AND CDO AS THE MATERIAL FILLING ITS REGION 2.

Material	Resonance Shift (nm)	Sensitivity (nm/RPU)	Linewidth (nm)	Sensitivity per linewidth (SPL)
AZO	70	700	39.5	17.7
CdO	125	1250	50	25.0

the variation of the real part of CdO's permittivity with respect to the wavelength is flatter than AZO's. Consequently, a CSS with CdO filling Region 2 would have a larger sensitivity than one filled with AZO. The sensitivity of the resonance wavelength to the real and imaginary parts of the permittivities of these two materials was tested with the final configuration, which is shown in Fig. 10 below. The associated resonant absorption results are illustrated in Fig. 3(b). When the dielectric constant of the material in Region 1 varies from 1 to 1.1, the AZO-based and CdO-based CSSs have the wavelengths of their resonant absorption peaks shifted from 1.931 to 2.001 μm and from 4.615 to 4.741 μm, respectively. The resultant sensing performance for each are calculated and compared in Table I. It is clear that the CSS with CdO adopted as the dispersive ENG material provides the higher sensitivity. Moreover, it also has a larger sensitivity per linewidth (SPL), which is defined as the ratio of wavelength sensitivity to the full-width at half maximum (FWHM) of the resonance peak. Both the sensitivity and SPL values are used to evaluate the sensing performance. Due to its predicted substantially better sensing performance, CdO was selected as the dispersive ENG material to commence the optimization of the sensor design for operation at mid-IR wavelengths in this work.

IV. DEVELOPING AND OPTIMIZING THE SENSOR CONFIGURATION

The CSS theory and the resulting sensitivity calculations are used to guide the evolution of the idealized fiber-based sensor configurations presented in Fig. 4. As will be discussed, the suspended fiber structure, Configuration 3 shown in Fig. 7, was found to be a much more practical sensor design. A modification of it, Configuration 4 shown in Fig. 10, has similar performance and should be the easiest one to actually realize in practice. Details of this microstructured fiber design evolution which led to this final configuration are presented.

A. Configuration 1

Four cylindrical core-shell structures were incorporated in the cladding of the PCF in our previous work [21] as shown in Fig. 4. The CSS elements were SiC-loaded air holes. Rectangular air holes were placed in the core region. They were initially used to introduce asymmetry in the refractive index distribution and, as a consequence, to achieve LWIR SPSM operation [27], [28]. Because of the complexity of the structure and the change in the operating wavelengths to the mid-IR, we began the design evolution by dramatically simplifying the structure to an ideal 3 region cylindrical CSS

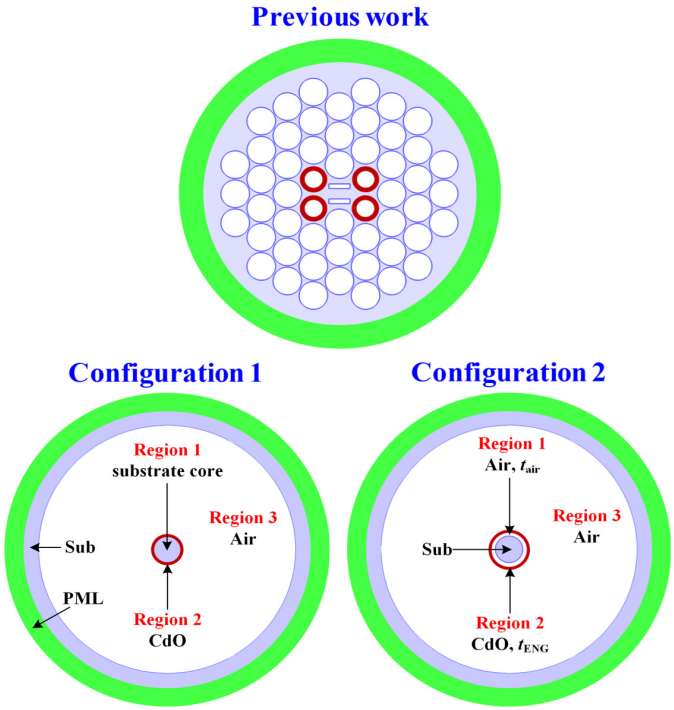

Fig. 4. Cross-sectional views of the structured fiber developed in [21] and those, Configurations 1 and 2, developed in this work.

surrounded by a substrate cylindrical wall that isolates it from the exterior.

As shown in Fig. 4, this Configuration 1 is composed of several concentric cylinders. The inner three layers, i.e., substrate, CdO, and air, constitute the ideal CSS and, hence, will enable the desired plasmonic resonance behavior. The substrate is chosen to be chalcogenide glass [29]. The real part of its permittivity is around 6.76 in the infrared wavelength range of interest, and its material loss is negligible in comparison to CdO. This CSS is wrapped by another layer of substrate to make it an idealized suspended core fiber.

The fiber configuration was simulated with the two-dimensional (2D) modelling environment in the Radio Frequency module of the commercial COMSOL software package [30]. It is a full-wave finite element method (FEM) based frequency domain solver of the Maxwell equations. The outer most shell represents the numerical absorbing boundary condition region, a perfect matched layer (PML). It, of course, is only present for the simulations. It is highlighted in green in all of the sufigures in Fig. 4. Region 1 of the CSS in Configuration 1 is now filled with the substrate and its Region 3 is filled with air. Consequently, the analyte to be sensed would now flow through Region 3. To obtain the sensitivity of this ideal suspended fiber, Eq. 7 must be modified to reflect the fact that the permittivity in Region 3 is changing rather than that in Region 1. Nevertheless, the same thinness requirement is maintained for Region 2 and the CSS solutions (6) remain the same. The sensitivity now becomes:

$$S = \frac{d(\lambda)}{d(Re(\varepsilon_3))} = \frac{d(\lambda)}{d(Re(\varepsilon_2))} \times \frac{d(Re(\varepsilon_2))}{d(Re(\varepsilon_3))} = B_2 \times \frac{A+1}{A-1}, \quad (9)$$

This indicates that by flowing the analytes through Region 3 of the CSS, the attained sensitivity is theoretically the same as flowing them through Region 1 of the version shown in Fig. 1. Therefore, this simple, ideal Configuration 1 also has the capabilities to act as a sensor when either a gas or liquid flows through its air region.

B. Configuration 2

It is clear by comparing Eqs. 7 and 9 that by filling either Region 1 or Region 3 of the CSS with an analyte to be sensed, the sensitivity will be the same. This leads to the important observation that if both Regions 1 and 3 are both filled with the same material to be detected so that $\varepsilon_1 = \varepsilon_3$, then the sensitivity becomes

$$S = 2B_2 \times \frac{A+1}{A-1}, \tag{10}$$

i.e., it doubles. Therefore, a configuration in which a CSS can be incorporated that allows for the flow of the material to be detected to go through both Regions 1 and 3 simultaneously will have double the sensitivity.

Therefore, Configuration 2 shown in Fig. 4 has an extra air layer in it that is introduced between the dispersive CdO ring and the fiber core to allow the material being sensed to flow in both air-filled regions. The extra air layer now serves as Region 1 of the CSS rather than fiber core. The substrate core of the fiber is not considered to be part of the CSS. While a 4 region CSS model could be developed that includes the substrate filled fiber core, the analytical solutions of the 3 region model were found to be a very satisfactory guide for the numerical optimizations of the final structured fiber configuration.

This doubling of the sensitivity outcome was validated with simulations. Fig. 5 illustrates the resonances of the fiber Configuration 2 with different cases when Regions 1 and 3 are filled materials of different permittivities. As anticipated from the analysis, when both Regions 1 and 3 are filled with a material having the relative permittivity ε = 1.1, the wavelength shift is significantly improved. It is more than double its value when compared to the other two cases in which only one region is filled with the material under test.

The key design parameters of Configuration 2 that can influence its performance are the thickness of the ENG and air layers, which are donated by t_{ENG} and t_{air}, respectively. The loss performance of the FM for different t_{ENG} and t_{air} values is shown in Figs. 6(a) and 6(b). One finds that the total loss can be adjusted by changing both t_{ENG} and t_{air}. In particular, the total loss increases as t_{ENG} and t_{air} decrease. These effects arise because those variations affect the portion of the E-field that is distributed in the ENG layer. While a larger t_{air} reduces the resonance effect and significantly broadens its linewidth, t_{ENG} variations adjust the resonance wavelength. The latter occurs because the ε_{ENG} value required by the resonance condition is changed. Considering the effects of both the loss magnitude and linewidth, t_{ENG} and t_{air} are selected to be 200 nm and 0.6 μm, respectively.

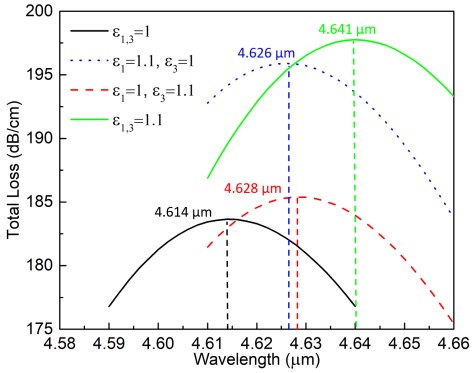

Fig. 5. Total loss of the fundamental mode of Configuration 2 for different cases in which Regions 1 and 3 are loaded with media having different relative permittivity values.

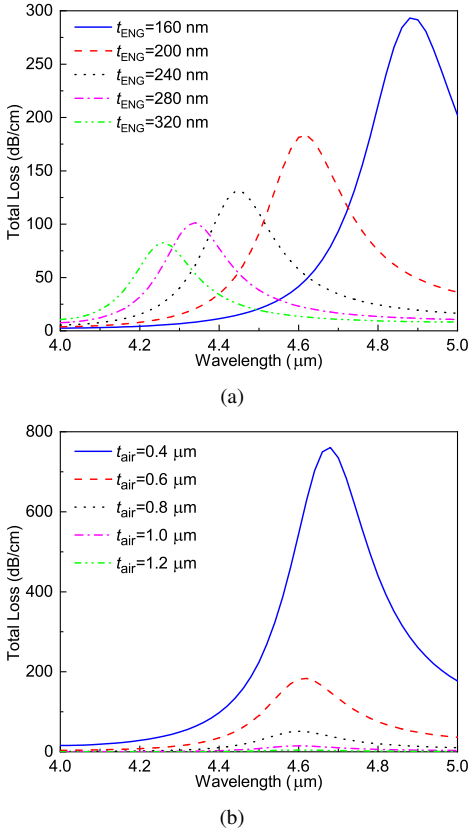

Fig. 6. Simulation studies of the key design parameters of Configuration 2. (a) Total loss of the FM for different ENG thickness, t_{ENG}, while the remaining design parameters are fixed as d_1 = 4.0 μm and t_{air} = 0.6 μm. (b) Total loss of the FM for different air layer thickness, t_{air}, while the remaining design parameters are fixed as d_1 = 4.0 μm and t_{ENG} = 200 nm.

C. Configuration 3

To make the ideal suspended fiber Configuration 2 realistic, three supporting arms are added to make Configuration 3, which is shown in Fig. 7. Moreover, note that there are three small air holes introduced in the center of the arms at the interface of each arm and the core. As will be demonstrated below, they are critical because they suppress the higher order modes (HOMs).

It is important to realize that the HOMs play a major

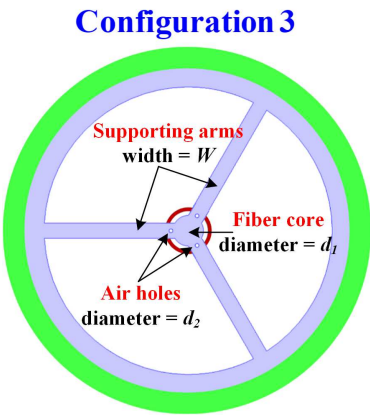

Fig. 7. Cross-sectional view of the suspended fiber, Configuration 3, in which three supporting arms enhance its mechanical stability.

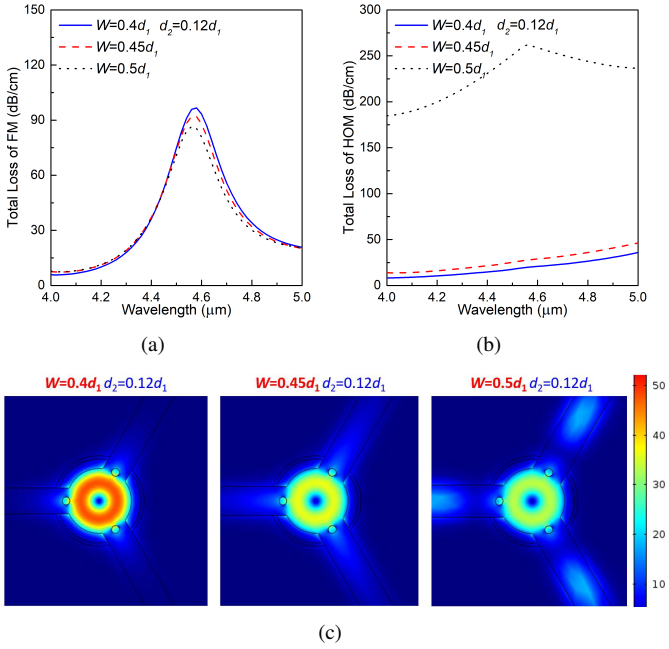

Fig. 8. Total loss of the (a) FM and (b) HOMs of the Configuration 3 fiber for different values of the arm width W. (c) Electric field distributions of only the HOMs for these cases.

role in the performance of any structure fiber. The previous simulation results shown in Figs. 3 and 5 only included the presences of the fundamental mode (FM). In fact, HOMs are excited in those structures as well and do lead to inaccurate sensing results based only the presence of the FM. It has been determined that by adjusting the width of the supporting arms, W, and the diameter of the air holes, d_2, the HOMs are well suppressed.

Figs. 8(a) and 8(b) show the simulated values of the total loss of the CSS-based suspended fiber for different values of W when the FM and HOMs are present. The hole diameter in these simulations was $d_2 = 0.12d_1$ with $d_1 = 4.0$ μm. It is clear from these results that a larger W reduces the loss of the FM and increases the loss of the HOMs. In particular, when $W = 0.5d_1$, the loss of the HOMs is much higher than that of the FM, i.e., over 150 dB/cm around the resonance wavelength.

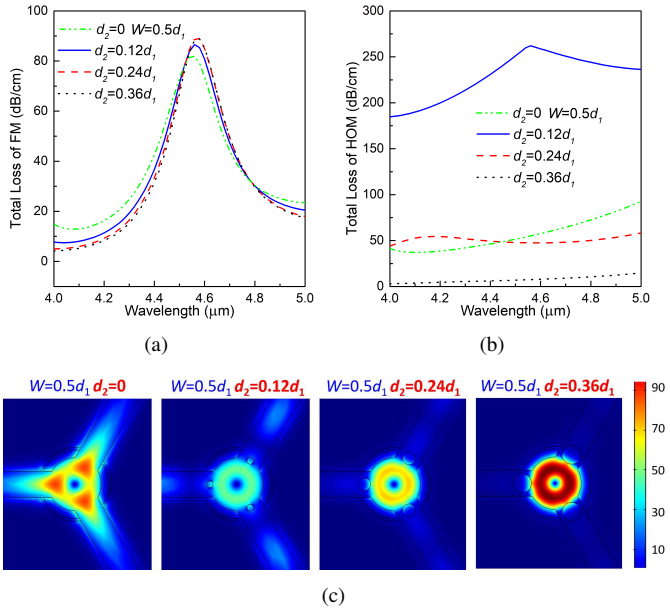

Fig. 9. Total loss of the (a) FM and (b) HOMs of the Configuration 3 fiber for different values of the hole diameter d_2. (c) Electric field distributions of only the HOMs for these cases.

This is due to the fact that with the increase of W, the electric field distribution of the HOMs is transferred from the core to the arms as shown in Fig. 8(c). This transference stimulates the rapid decay of the HOMs and, consequently, they can be nearly completely suppressed over very modest fiber lengths. However, W cannot be too wide since the resonance becomes detuned and this effect reduces the SPL. Therefore, W was selected to be $0.5d_1$ for the optimized design.

The diameter d_2 of the three air holes is another key factor that determines the loss of the HOMs. Parameter studies to determine its optimal value were performed with the arm width set to the optimal value $W = 0.5d_1$. According to the simulated results shown in Fig. 9(a), there is only a minor effect on the total loss of the FM when the diameter of the small air holes is changed. On the other hand, its variation causes some noticeable changes in the HOM total loss results as shown in Fig. 9(b). Note that these two subfigures have substantially different scales on their y-axes. As observed in Fig. 9(c), the electric field of the HOMs is well confined in the core area when the air holes are large so they experience relatively lower total loss. As d_2 is reduced, the electric field distribution is transferred from the core to the arms and the HOMs experience a much higher total loss. Notice, however, that if these air holes are completely removed, i.e., with d_2 = 0, the electric fields are redistributed back into the edges of the core area where the arms intersect it. This effect arises because the low-index regions, i.e., the air holes in the substrate, are no longer present to isolate the core region. Given the substantially larger total loss of the HOMs in the $d_2 = 0.12d_1$ case, it was selected for the optimized design.

D. Final Configuration

Finally, design modifications were considered to reduce the fabrication complexity of the suspended fiber. The cylindri-

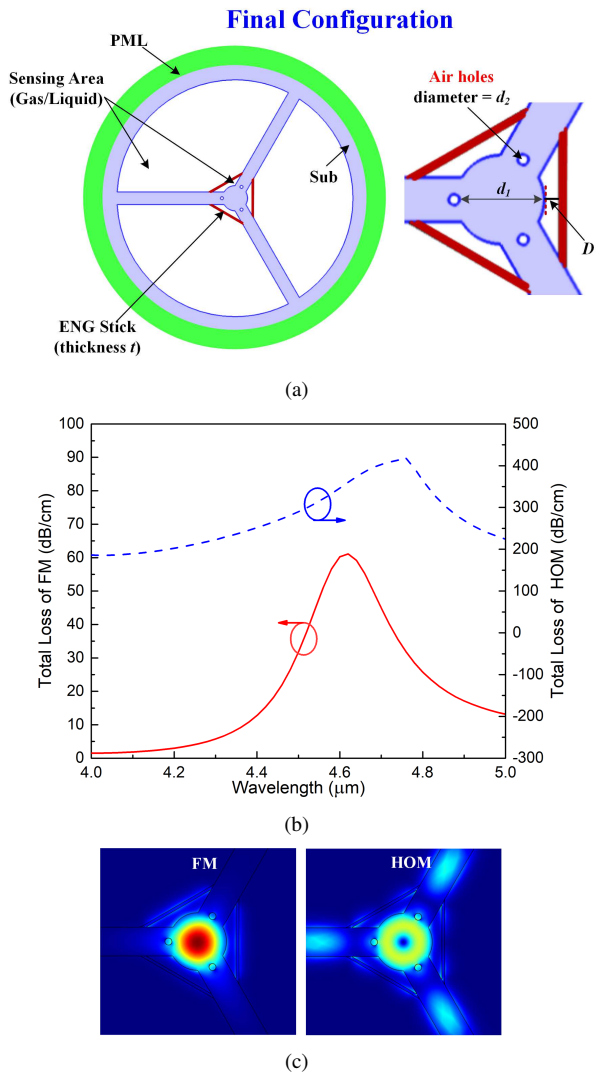

Fig. 10. Optimized CSS-based suspended core fiber. (a) Cross section view of the Final Cconfiguration. (b) Total loss of the FM and HOMs as functions of the source wavelength. (c) Electric field distributions of the FM and HOMs at the resonance wavelength, 4.62 μm.

cal ENG pieces shown in the previous configurations were replaced by straight ENG segments. The final configuration is shown in Fig. 10(a). The straight ENG segments would be much easier to fabricate and insert into the fiber. Parameter studies determined that the performance of this suspended fiber was not significantly different in comparison to that of Configuration 3.

The configuration was then optimized with overall considerations to maximize the sensitivity, SPL, and HOM suppression. The optimized design parameters of the Final Configuration shown in Fig. 10(a) were determined to be d_1 = 4.0 μm, t_{ENG} = 200 nm, D = 0.6 μm, $W = 0.5d_1$, and $d_2 = 0.12d_1$. The resultant simulated total losses of the FM and HOMs of the fiber are plotted in Fig. 10(b). It is observed that the total loss of the FM at the resonance wavelength is below 100 dB/cm while the loss difference between the HOM and FMs is over 300 dB/cm. The electric field distribution of the FM and HOMs are also presented in Figs. 10(c) and 10(d), respectively.

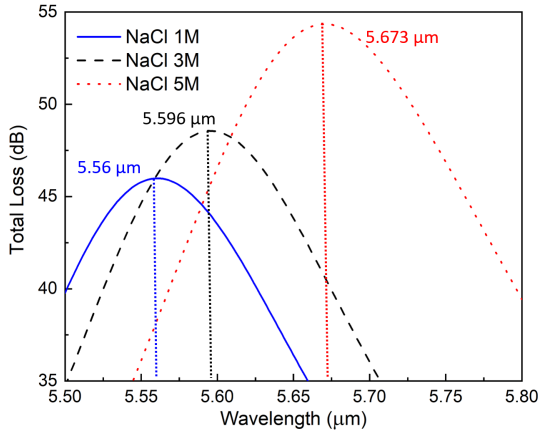

Fig. 11. Resonance peak shift when the air in Regions 1 and 3 and the three small air holes of a 1.0 mm length of the optimized CSS-based suspended core fiber is replaced with three different liquids with the indicated NaCl concentrations. The absorption peak wavelengths for each case are specifically identified.

Within the detection range from 1.0 to 1.01, the calculated sensitivity and SPL values for such a fiber sensor whose length is 5.0 mm are 1250 nm/RPU and 31.4, respectively.

V. Sensing Application

It was found that there is little difference in the resonance shifts whether only Regions 1 and 3 were filled with the solution or they and all three of the small air holes in the arms were. Consequently, the following results were obtained for a 1.0 mm length of the suspended CSS-based core fiber with Regions 1, 3, and all three small air holes filled with the analyte. As discussed above, the peak of the excited CSS-based plasmonic resonance is very sensitive to the relative permittivity of the medium filling the air regions.

One possible environmental monitoring application for the optimized design follows from the one considered in [21], i.e., for detecting the concentration of the salt NaCl in water, but now in the mid-IR range. Three NaCl solutions with different concentrations [31] and, hence, different relative permittivity values were considered. Despite being small relative to the losses in the ENG material, the material absorption losses of these solutions were included in all of the sensor performance simulations. The material dispersion of the CdO was also taken into account. The dispersion data was selected for the CdO being at room temperature and under standard atmospheric pressure. The resulting resonance peaks of the FM for these three analytes in a 1.0 mm-length of the CSS-based suspended core fiber sensor are shown in Fig. 11. The results clearly show the resonance peak is red-shifted as the NaCl concentration increases. While these signal levels are quite low, they are easily detected with an optical spectrum analyser. Longer lengths, e.g., 5.0 mm, do not affect the resonance wavelength or overall sensitivity, but they do increase the total loss substantially and the SPL values by small amounts. Comparisons of the lossless and lossy material simulations show much smaller nanometer variations in the resonance wavelength.

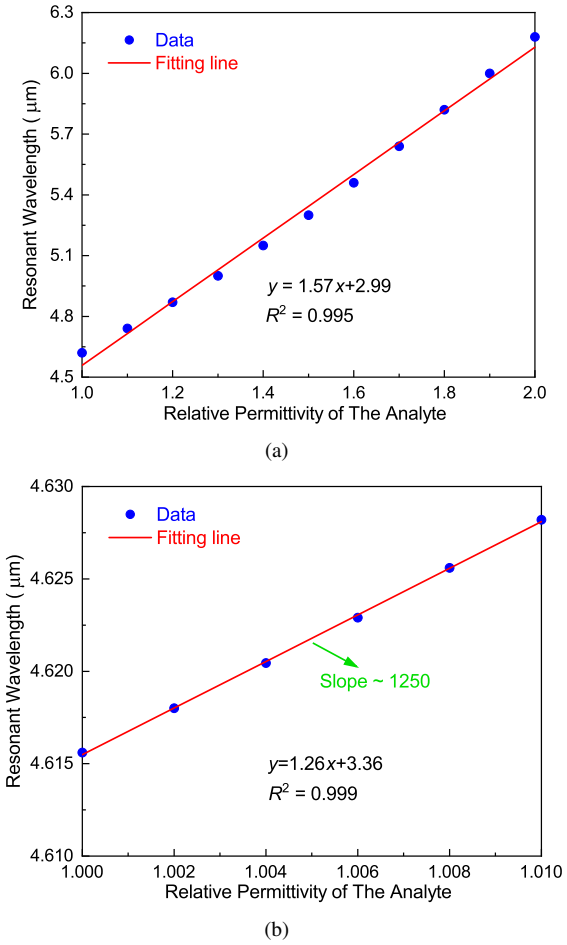

Fig. 12. Detection range of the CSS-based suspended fiber sensor as a function of the relative permittivity of the analyte. (a) General large range for either liquid or gas monitoring. (b) Zoom-in range for gas monitoring. The linear equation fit to the simulation data was obtained by regression analysis with the indicated R^2 coefficient of determination.

The variation of the resonance wavelength as a function of the relative permittivity of the medium filling the air regions of the fiber over a wide range of values is plotted in Fig. 12(a). The mid-IR fiber sensor has a relatively large and useful detection range, i.e., from 1.0 to 2.0. This range indicates that the CSS-based suspended core fiber can be utilized as a mid-IR sensor not only for liquids but also for gases. In fact, as shown in Fig. 12(b), the resonance wavelength changes linearly from 4.6151 to 4.6276 μm as the permittivity of the analytes changes from 1.0 to 1.01. These results correspond to an overall 12.5 nm shift which readily measured and is very adequate for monitoring gases with a very compact device.

Finally, the sensitivity of the optimized design is calculated from the results presented in Fig. 12 to be 1250 and 1700 nm/RPU for gas (ϵ_{gas}, 1.0 to 1.01) and liquid (ϵ_{liquid}, 1.5 to 1.7) detection, respectively. However, it is more conventional to express the sensitivity in terms of refractive index units (RIU). Thus, the corresponding values are 2510 and 4303 nm/RIU, respectively. Another important factor is the sensitivity per linewidth. It actually changes with the length of the fiber [21]. For the presented cases with a 1.0 mm length of the designed fiber sensor, the calculated SPL is 9.7 and 53.1 for the gas and liquid applications, respectively.

The developed CSS-based suspended core fiber is compared with comparable state-of-the-art sensors in Table 2. The values of the sensitivity and SPL, as well as the refractive index range of the analyte, are given along with the interaction (fiber) length. It is noted that the wavelength sensitivity is better than those reported in [32], [33], [34], [35], [36], [37], [19], [20], [38] and comparable to the best one [18]. On the other hand, the SPL and the detection range values are superior. Furthermore, the required interaction length is quite short (millimeter level) and the measurement inaccuracy introduced by the higher order modes has been eliminated, which is not the case in most references. Moreover, calculations based on the data in [39], [40] of the nonlinear contributions to the refractive index variations associated with a typical chalcogenide glass microstructured optical fiber (MOF) indicate that they are negligible over this short interaction length in comparison to those introduced by the analytes and, hence, were neglected. Another important issue is that by selecting a different ENG material, e.g., AZO [24], the working wavelength of the developed fiber sensor can be shifted from the mid-IR to near-IR wavelengths. Simulations have confirmed that there is only a small decrease in the sensitivity at those shorter wavelengths.

While we do not have access to any fabrication and measurement facilities to build and test a prototype of our design,we are nevertheless quite confident that it could be realized. Hybrid MOFs and their applications have advanced in recent years because of the development of exceptional fabrication technologies. A variety of structural designs [41] and material compositions [42], [43] have been realized successfully that are more complex than our developed design. The preform needed to construct a MOF such as the one that would be needed for our design can be realized, for example, through stacking [44], drilling [45], die extrusion [46], or 3-D printing methods [47]. Combinations of ENZ-ENG materials in structured fibers have been investigated theoretical and experimentally [48], [49]. The ENG thin segments near the fiber core required in our final recommended design can be accomplished with high-pressure chemical vapor deposition [50], [51].

Moreover, suspended-core optical fibers are an established MOF configuration. Chalcogenide glass suspended-core fibers have been realized even for smaller near-infrared wavelengths [52], [53]. Suspended-core MOFs for liquid and gas sensors have been accomplished, e.g., [54], [55]. In fact, indium tin oxide (ITO) thin films have been deposited in a silica suspended-core MOF by sputtering for near-infrared gas sensing [56]. Even the same type of small hole in the suspended core required for our design was also attained. With the increasing numbers of researchers being attracted to ENZ-ENG materials and their optical applications [57], more advances in materials and implementation methods will be available in the near future. They would further help accomplish the eventual fabrication of the developed sensor design and facilitate the realization of its attractive performance characteristics. Furthermore, a practical system will require a suitable light source. One can be realized by splicing the single mode suspended-core fiber with a standard single mode fiber through a properly designed

TABLE II
COMPARISONS OF THE DEVELOPED CSS-BASED SUSPENDED-CORE FIBER SENSOR AND COMPARABLE STATE-OF-THE-ART FIBER-BASED DEVICES.

References	Sensitivity (nm/RIU)	Refractive index detection range	SPL	Interaction length (mm)
[32]	252	1.33-1.38	83	30
[33]	260.8	1.333-1.373	33	40
[34]	199	1.336-1.371	19	1.9
[35]	286.2	1.33-1.39	14	23
[36]	428.1	1.317-1.445	-	20
[37]	510	1.59-1.61	320	0.01
[19]	596	1.00-1.05	7.5	-
[20]	500	1.00-1.30	4.5	-
[38]	1500	1.33-1.45	-	20
[18]	5500	1.23-1.29	-	-
[21]	566.6	1.00-1.41	35.4	5.0
This work	2510-4303	1.00-1.41	9.7-53.1	1.0

taper [58]. Alternatively, a wide band supercontinuum source realized as a suspended core fiber [59], [60] could be matched directly to it.

VI. CONCLUSION

In this work, a core-shell structure (CSS)-based suspended fiber sensor was developed for the first time for gas and liquid monitoring in the mid-IR wavelength range. The theory of the CSS plasmonic absorption resonance was exploited to maximize the sensor's performance. It indicated an ENG medium was necessary to realize the resonance. Both AZO and CdO were considered as the plasmonic material, and CdO was found to have more attractive properties for our application. An evolution of CSS-based microstructure fiber designs, which led to the final, more readily realizable, mechanically stable, and highest sensitivity configuration, was then presented. Parameter studies were described to demonstrate how the optimized design parameters were selected and what total loss outcomes were realized with them. It was shown how the final configuration eliminated the higher order modes (HOMs) in favour of the fundamental mode (FM) to enhance the sensor's sensitivity and SPL values. The sensing capability of the optimized CSS-based suspended core fiber with a fixed, short length was illustrated with both liquid and gas examples. Finally, the performance characteristics of the developed mid-IR sensor were compared with reported state-of-the-art fiber-based sensors. Its superior sensing performance characteristics suggest that it is an ideal candidate for the development of small, portable environmental monitoring devices.

REFERENCES

[1] B. Culshaw, "Optical fiber sensor technologies: Opportunities and-perhaps-pitfalls," *Journal of Lightwave Technology*, vol. 22, no. 1, pp. 39–50, 2004.

[2] D. Wu, Y. Zhao, and J. Li, "PCF taper-based Mach-Zehnder interferometer for refractive index sensing in a PDMS detection cell," *Sensors and Actuators B Chemical*, vol. 213, pp. 1–4, 2015.

[3] T. Zhu, D. Wu, M. Liu, and D. W. Duan, "In-line fiber optic interferometric sensors in single-mode fibers," *Sensors (Basel, Switzerland)*, vol. 12, no. 8, pp. 10 430–10 449, 2012.

[4] Y. Zhang, C. Shi, C. Gu, L. Seballos, and J. Z. Zhang, "Molecular probe based on photonic crystal fiber (PCF) and surface enhanced Raman scattering (SERS)," in *2007 IEEE Sensors*, 2007, pp. 375–377.

[5] O. Frazao, J. M. Baptista, and J. L. Santos, "Temperature-independent strain sensor based on a Hi-Bi photonic crystal fiber loop mirror," *IEEE Sensors Journal*, vol. 7, no. 10, pp. 1453–1455, 2007.

[6] H. Jiri, S. S. Yee, and G. Gunter, "Surface plasmon resonance sensors: Review," *Analytical and Bioanalytical Chemistry*, vol. 377, no. 3, pp. 528–39, 1999.

[7] Z. Hui, G. Shecheng, L. Yunhan, C. Zhenshi, X. Songsong, W. Lei, H. Xincheng, H. Bingsen, F. Yuanhua, H. Miao, W. Liu, Z. Chen, and Z. Li, "Ultrasensitive Mach-Zehnder interferometric temperature sensor based on liquid-filled D-shaped fiber cavity," *Sensors*, vol. 18, no. 4, 2018.

[8] T. Li, X. Dong, C. C. Chan, K. Ni, S. Zhang, and P. P. Shum, "Humidity sensor with a PVA-coated photonic crystal fiber interferometer," *IEEE Sensors Journal*, vol. 13, no. 6, pp. 2214–2216, 2013.

[9] A. D. Kersey, T. A. Berkoff, and W. W. Morey, "Multiplexed fiber Bragg grating strain-sensor system with a fiber Fabry-Perot wavelength filter," *Optics Letters*, vol. 18, no. 16, pp. 1370–1373, 1993.

[10] P. T. Snee, R. C. Somers, G. Nair, J. P. Zimmer, M. G. Bawendi, and D. G. Nocera, "A ratiometric CdSe/ZnS nanocrystal pH sensor." *Journal of the American Chemical Society*, vol. 128, no. 41, p. 13320, 2015.

[11] M. Morshed, M. Imran Hassan, T. K. Roy, M. S. Uddin, and S. M. Abdur Razzak, "Microstructure core photonic crystal fiber for gas sensing applications," *Applied Optics*, vol. 54, no. 29, pp. 8637–8643, 2015.

[12] D. J. Monsma, J. C. Lodder, T. J. A. Popma, and B. Dieny, "Perpendicular hot electron spin-valve effect in a new magnetic field sensor: The spin-valve transistor," *Physical Review Letters*, vol. 74, no. 26, pp. 5260–5263, 1995.

[13] A. Iadicicco, A. Cusano, A. Cutolo, R. Bernini, and M. Giordano, "Thinned fiber Bragg gratings as high sensitivity refractive index sensor," *IEEE Photonics Technology Letters*, vol. 16, no. 4, pp. 1149–1151, 2004.

[14] Z. Tian, S. H. Yam, and H. P. Loock, "Refractive index sensor based on an abrupt taper Michelson interferometer in a single-mode fiber," *Optics Letters*, vol. 33, no. 10, pp. 1105–1107, 2008.

[15] Y. Yao, B. Yi, J. Xiao, and Z. H. Li, "Surface plasmon resonance biosensors and its application," in *International Conference on Bioinformatics and Biomedical Engineering*, 2007.

[16] O. Cooper, B. Wang, C. L. Brown, J. Tiralongo, and F. Iacopi, "Toward label-free biosensing with silicon carbide: A review," *IEEE Access*, vol. 4, no. 1, pp. 477–497, 2016.

[17] N. Paliwal and J. John, "Theoretical modeling and investigations of AZO coated LMR based fiber optic tapered tip sensor utilizing an additional TiO_2 layer for sensitivity enhancement," *Sensors and Actuators B Chemical*, vol. 238, pp. 1–8, 2017.

[18] C. Liu, L. Yang, X. Lu, Q. Liu, and P. K. Chu, "Mid-infrared surface plasmon resonance sensor based on photonic crystal fibers," *Optics Express*, vol. 25, no. 13, pp. 14 227–14 237, 2017.

[19] Z. Zhang, L. Luo, C. Xue, W. Zhang, and S. Yan, "Fano resonance based on metal-insulator-metal waveguide-coupled double rectangular cavities for plasmonic nanosensors," *Sensors*, vol. 16, no. 642, 2016.

[20] M. Turdev, I. H. Giden, C. Babayigit, Z. Hayran, E. Bor, C. Boztug, H. Kurt, and K. Staliunas, "Mid-infrared T-shaped photonic crystal waveguide for optical refractive index sensing," *Sensors and Actuators B: Chemical*, vol. 245, pp. 765–773, 2017.

[21] T. Yang, C. Ding, R. W. Ziolkowski, and Y. J. Guo, "A controllable plasmonic resonance in a SiC-loaded single-polarization single-mode

photonic crystal fiber enables its application as a compact LWIR environmental sensor," *Materials*, vol. 13, no. 3915, 2020.

[22] S. Arslanagic, R. W. Ziolkowski, and O. Breinbjerg, "Analytical and numerical investigation of the radiation from concentric metamaterial spheres excited by an electric Hertzian dipole," *Radio Science*, vol. 42, no. 6, 2016.

[23] S. Arslanagic, Y. Liu, R. Malureanu, and R. W. Ziolkowski, "Impact of the excitation source and plasmonic material on cylindrical active coated nano-particles," *Sensors*, vol. 11, no. 9, 2011.

[24] G. V. Naik, V. M. Shalaev, and A. Boltasseva, "Alternative plasmonic materials: Beyond gold and silver," *Advanced Materials*, vol. 25, no. 24, 2013.

[25] Q. Guo, Y. Cui, Y. Yao, Y. Ye, Y. Yang, X. Liu, S. Zhang, X. Liu, J. Qiu, and H. Hosono, "A solution-processed ultrafast optical switch based on a nanostructured epsilon-near-zero medium," *Advanced Materials*, vol. 29, no. 27, p. 1700754, 2017.

[26] E. Sachet, C. T. Shelton, J. S. Harris, B. E. Gaddy, D. L. Irving, S. Curtarolo, B. F. Donovan, P. E. Hopkins, P. A. Sharma, A. L. Sharma, J. Ihlefeld, S. Franzen, and J.-P. Maria, "Dysprosium-doped cadmium oxide as a gateway material for mid-infrared plasmonics," *Nature Materials*, vol. 14, no. 4, pp. 414–420, 2015.

[27] T. Yang, E. Wang, H. Jiang, Z. Hu, and K. Xie, "High birefringence photonic crystal fiber with high nonlinearity and low confinement loss," *Optics Express*, vol. 23, no. 7, pp. 8329–8337, 2015.

[28] T. Yang, C. Ding, R. W. Ziolkowski, and Y. J. Guo, "A scalable THz photonic crystal fiber with partially-slotted core that exhibits improved birefringence and reduced loss," *Journal of Lightwave Technology*, vol. 36, no. 16, pp. 3408–3417, 2018.

[29] B. Zhang, W. Guo, Y. Yu, C. Zhai, S. Qi, A. Yang, L. Li, Z. Yang, R. Wang, D. Tang, G. Tao, B. Luther-Davies, and P. Lucas, "Low loss, high NA chalcogenide glass fibers for broadband mid-infrared supercontinuum generation," *Journal of the American Ceramic Society*, vol. 98, no. 5, pp. 1389–1392, 2015.

[30] COMSOL-Multiphysics, "Comsol, Stockholm, Sweden," http://cn.comsol.com/rf-module.

[31] J. E. Bertie, M. K. Ahmed, and H. H. Eysel, "Infrared intensities of liquids. 5. Optical and dielectric constants, integrated intensities, and dipole moment derivatives of H_2O and D_2O at 22° C," *The Journal of Physical Chemistry*, vol. 93, no. 6, pp. 2210–2218, 1989.

[32] Y. Zhao, X. G. Li, L. Cai, and Y. Yang, "Refractive index sensing based on photonic crystal fiber interferometer structure with up-tapered joints," *Sensors and Actuators B Chemical*, vol. B221, pp. 406–410, 2015.

[33] Q. Wang, L. Kong, Y. Dang, F. Xia, Y. Zhang, Y. Zhao, H. Hu, and J. Li, "High sensitivity refractive index sensor based on splicing points tapered SMF-PCF-SMF structure Mach-Zehnder mode interferometer," *Sensors and Actuators B Chemical*, vol. 225, pp. 213–220, 2016.

[34] M. Deng, X. Sun, H. Wei, and J. Li, "Photonic crystal fiber-based modal interferometer for refractive index sensing," *Photonics Technology Letters*, vol. 26, no. 6, pp. 531–534, 2014.

[35] Y. Zhao, L. Cai, X.-G. Li, and F.-C. Meng, "Liquid concentration measurement based on SMS fiber sensor with temperature compensation using an FBG," *Sensors and Actuators B: Chemical*, vol. 196, pp. 518–524, 2014.

[36] Y. H. Zhou, Q. X. Guang, I. M. Rajibul, L. Kok-Sing, and H. Ahmad, "Simultaneous measurement of aliphatic alcohol concentration and temperature based on etched taper FBG," *Sensors and Actuators B: Chemical*, vol. 202, pp. 959–963, 2014.

[37] Z.-N. Farzad and S. Reza, "Hybrid graphene-molybdenum disulphide based ring resonator for label-free sensing," *Optics Communications*, vol. 371, pp. 9–14, 2016.

[38] Y.-F. Chou, C.-T. C. Chao, H. J. Huang, N. T. R. N. Kumara, and H.-P. Chiang, "Ultra-high refractive index sensing structure based on a metal-insulator-metal waveguide-coupled T-shape cavity with metal nanorod defects," *Nanomaterials*, vol. 9, no. 10, p. 1433, 2019.

[39] Y. Yu, X. Gai, P. Ma, D. Y. Choi, Z. Yang, R. Wang, S. Debbarma, S. J. Madden, and B. Luther-Davies, "A broadband, quasi-continuous, mid-infrared supercontinuum generated in a chalcogenide glass waveguide," *Laser and Photonics Reviews*, vol. 8, no. 5, pp. 792–798, 2015.

[40] F. M. R. Karim, B. M. A. Rahman, and G. P. Agrawl, "Mid-infrared supercontinuum generation using dispersion-engineered $ge_{11.5}as_{24}se_{64.5}$ chalcogenide channel waveguide." *Optics Express*, vol. 23, no. 5, pp. 6903–6914, 2015.

[41] M. A. Schmidt, A. Argyros, and F. Sorin, "Hybrid optical fibers - An innovative platform for in-fiber photonic devices," *Advanced Optical Materials*, vol. 4, pp. 13–36, 2016.

[42] S. A. J. Cerqueira, F. Luan, C. M. Cordeiro, A. K. George, and J. C. Knight, "Hybrid photonic crystal fiber," *Optics Express*, vol. 14, no. 2, pp. 926–931, 2006.

[43] V. Pacheco-Pena, N. Engheta, S. Kuznetsov, A. Gentselev, and M. Beruete, "Experimental realization of an epsilon-near-zero graded-index metalens at terahertz frequencies," *Physical Review Applied*, vol. 8, no. 3, pp. 034 036–10, 2017.

[44] P. S. J. Russell, "Photonic-crystal fibers," *Journal of Lightwave Technology*, vol. 24, no. 12, pp. 4729–4749, 2006.

[45] K. Nielsen, H. K. Rasmussen, A. J. L. Adam, P. C. M. Planken, and P. U. Jepsen, "Bendable, low-loss Topas fibers for the terahertz frequency range," *Optics Express*, vol. 17, no. 10, pp. 8592–8601, 2009.

[46] S. Atakaramians, A. V. Shahraam, H. Ebendorff-Heidepriem, M. Nagel, and T. M. Monro, "THz porous fibers: Design, fabrication and experimental characterization," *Optics Express*, vol. 17, no. 16, pp. 14 053–14 062, 2009.

[47] K. Cook, J. Canning, S. Leon-Saval, Z. Reid, M. A. Hossain, J.-E. Comatti, Y. Luo, and G.-D. Peng, "Air-structured optical fiber drawn from a 3D-printed preform," *Optics Letters*, vol. 40, no. 17, pp. 3966–3969, 2015.

[48] J. Yang, I. Ghimire, P. C. Wu, S. Gurung, C. Arndt, D. P. Tsai, and H. W. H. Lee, "Photonic crystal fiber metalens," *Nanophotonics*, vol. 8, no. 3, pp. 443–449, 2019.

[49] K. Minn, A. Anopchenko, J. Yang, and H. W. H. Lee, "Excitation of epsilon-near-zero resonance in ultra-thin indium tin oxide shell embedded nanostructured optical fiber," *Scientific Reports*, vol. 8, p. 2342, 2018.

[50] A. Amezcua-Correa, J. Yang, C. E. Finlayson, A. C. Peacock, J. R. Hayes, P. J. A. Sazio, J. J. Baumberg, and S. M. Howdle, "Surface-enhanced Raman scattering using microstructured optical fiber substrates," *Advanced Functional Materials*, vol. 17, no. 13, pp. 2024–2030, 2007.

[51] R. He, P. J. A. Sazio, A. C. Peacock, N. Healy, J. R. Sparks, M. Krishnamurthi, V. Gopalan, and J. V. Badding, "Integration of gigahertz-bandwidth semiconductor devices inside microstructured optical fibres," *Nature Photonics*, vol. 6, no. 3, pp. 174–179, 2012.

[52] M. El-Amraoui, J. Fatome, J.-C. Jules, B. Kibler, G. Gadret, C. Fortier, F. Smektala, I. Skripatchev, C. Polacchini, Y. Messaddeq *et al.*, "Strong infrared spectral broadening in low-loss As-S chalcogenide suspended core microstructured optical fibers," *Optics Express*, vol. 18, no. 5, pp. 4547–4556, 2010.

[53] W. Gao, M. El Amraoui, M. Liao, H. Kawashima, Z. Duan, D. Deng, T. Cheng, T. Suzuki, Y. Messaddeq, and Y. Ohishi, "Mid-infrared supercontinuum generation in a suspended-core As_2S_3 chalcogenide microstructured optical fiber," *Optics Express*, vol. 21, no. 8, pp. 9573–9583, 2013.

[54] T. Nemecek, M. Komanec, T. Martan, R. Ahmad, and S. Zvanovec, "Suspended-core microstructured fiber for refractometric detection of liquids," *Applied Optics*, vol. 54, no. 30, pp. 8899–8903, 2015.

[55] T. Martan, J. Aubrecht, O. Podrazkỳ, V. Matějec, and I. Kašík, "Detection of hydrocarbons using suspended core microstructured optical fiber," *Sensors and Actuators B: Chemical*, vol. 202, pp. 123–128, 2014.

[56] D. Lopez-Torres, A. Lopez-Aldaba, C. Elosua, J. L. Auguste, R. Jamier, P. Roy, M. Lopez-Amo, and F. J. Arregui, "Comparison between different structures of suspended-core microstructured optical fibers for volatiles sensing," *Sensors*, vol. 18, no. 8, 2018.

[57] S. Gurung, A. Anopchenko, S. Bej, J. Joyner, J. D. Myers, J. Frantz, and H. W. H. Lee, "Atomic layer engineering of epsilon-near-zero ultrathin films with controllable field enhancement," *Advanced Materials Interfaces*, vol. 7, p. 2000844, 2020.

[58] K. Vanmol, T. Baghdasaryan, N. Vermeulen, K. Saurav, J. Watté, H. Thienpoint, and J. V. Erps, "3d direct laser writing of microstructured optical fiber tapers on single-mode fibers for mode-field conversion," *Optics Express*, vol. 28, no. 24, pp. 36 147–36 158, 2020.

[59] T. Cheng, Y. Kanou, X. Xue, D. Deng, and Y. Ohishi, "Mid-infrared supercontinuum generation in a novel $asse_2$-as_2s_5 hybrid microstructured optical fiber," *Optics Express*, vol. 22, no. 19, pp. 23 019–23 025, 2014.

[60] D. U. Moller, Y. Yu, I. Kubat, C. R. Petersen, X. Gai, L. Brilland, D. Mechin, C. Caillaud, J. Troles, B. Luther-Davies, and O. Bang, "Multi-milliwatt mid-infrared supercontinuum generation in a suspended core chalcogenide fiber." *Optics Express*, vol. 23, no. 3, pp. 3282–3291, 2015.

Tianyu Yang was born in Anhui Province, China, in 1990. He received a Bachelor degree and Master degree in Measurement and Control Technology from Hefei University of Technology, Hefei, China, in 2012 and 2016 respectively. He will receive the Ph.D. degree from University of Technology Sydney (UTS), Sydney, Australia in 2021. He has authored/co-authored 15 papers in peer-reviewed international journals. His current research interests include THz and optical photonic crystal fiber design and its sensing application.

He is currently a Research Fellow in Center for Opto-Electronic Engineering and Technology, Shenzhen Institute of Advanced Technology, Chinese Academy of Sciences.

Can Ding (M'2016) received the bachelor's degree in microelectronics from Xidian University, Xi'an, China, in 2009, and the Ph.D. degree from Macquarie University, Sydney, Australia, in 2015.

From 2012 to 2015, he was under the cotutelle agreement between Macquarie University and Xidian University. During this samesss period, he was also with Commonwealth Scientific and Industrial Research Organisation DPaS Flagship, Marsfield, Australia. From 2015 to 2017, he was an industrial-sponsored Post-Doctoral Research Fellow with the Global Big Data Technologies Centre, University of Technology Sydney, where he is currently a Lecturer. His research interest is in the area of base station antennas, reconfigurable antennas, phase shifters, and fibres for wireless communication and sensing. Dr. Ding is a recipient of the Australia Research Council Distinguish Early Career Researcher Award Fellow in 2020.

Richard W. Ziolkowski (M'87–SM'91–F'94-LF'2020) received the B. Sc. (magna cum laude) degree (Hons.) in physics from Brown University, Providence, RI, USA, in 1974; the M.S. and Ph.D. degrees in physics from the University of Illinois at Urbana-Champaign, Urbana, IL, USA, in 1975 and 1980, respectively; and an Honorary Doctorate degree from the Technical University of Denmark, Kongens Lyngby, Denmark in 2012.

Prof. Ziolkowski is the recipient of the 2019 IEEE Electromagnetics Award (IEEE Technical Field Award). He is a Fellow of the Optical Society of America (OSA, 2006) and the American Physical Society (APS, 2016). He served as the President of the IEEE Antennas and Propagation Society in 2005. He is also actively involved with the URSI, OSA and SPIE professional societies. He was the Australian DSTO Fulbright Distinguished Chair in Advanced Science and Technology from 2014-2015. He was a 2014 Thomas-Reuters Highly Cited Researcher.

He is currently a Distinguished Professor in the Global Big Data Technologies Centre in the Faculty of Engineering and Information Technologies (FEIT) at the University of Technology Sydney, Ultimo NSW, Australia. He became a Professor Emeritus at the University of Arizona in 2018, where he was a Litton Industries John M. Leonis Distinguished Professor in the Department of Electrical and Computer Engineering in the College of Engineering and was also a Professor in the College of Optical Sciences. He was the Computational Electronics and Electromagnetics Thrust Area Leader with the Engineering Research Division of the Lawrence Livermore National Laboratory before joining The University of Arizona, Tucson, AZ, USA, in 1990. His current research interests include the application of new mathematical and numerical methods to linear and nonlinear problems dealing with the interaction of electromagnetic and acoustic waves with complex linear and nonlinear media, as well as metamaterials, metamaterial-inspired structures, nano-structures, and other classical and quantum applications-specific configurations.

Y. Jay Guo (F'2014) received a Bachelor Degree and a Master Degree from Xidian University in 1982 and 1984, respectively, and a PhD Degree from Xian Jiaotong University in 1987, all in China. His research interest includes antennas, mm-wave and THz communications and sensing systems as well as big data technologies. He has published four books and over 550 research papers including 280 journal papers, most of which are in IEEE Transactions, and he holds 26 patents. He is a Fellow of the Australian Academy of Engineering and Technology, a Fellow of IEEE and a Fellow of IET, and was a member of the College of Experts of Australian Research Council (ARC, 2016-2018). He has won a number of most prestigious Australian Engineering Excellence Awards (2007, 2012) and CSIRO Chairman's Medal (2007, 2012). He was named one of the most influential engineers in Australia in 2014 and 2015, respectively, and one of the top researchers in Australia in 2020.

He is a Distinguished Professor and the Director of Global Big Data Technologies Centre (GBDTC) at the University of Technology Sydney (UTS), Australia. Prior to this appointment in 2014, he served as a Director in CSIRO for over nine years. Before joining CSIRO, he held various senior technology leadership positions in Fujitsu, Siemens and NEC in the U.K.

Prof Guo has chaired numerous international conferences and served as guest editors for a number of IEEE publications. He is the Chair of International Steering Committee, International Symposium on Antennas and Propagation (ISAP). He was the International Advisory Committee Chair of IEEE VTC2017, General Chair of ISAP2022, ISAP2015, iWAT2014 and WPMC'2014, and TPC Chair of 2010 IEEE WCNC, and 2012 and 2007 IEEE ISCIT. He served as Guest Editor of special issues on "*Low-Cost Wide-Angle Beam Scanning Antennas*", "*Antennas for Satellite Communications*" and "*Antennas and Propagation Aspects of 60-90GHz Wireless Communications*," all in IEEE Transactions on Antennas and Propagation, Special Issue on "*Communications Challenges and Dynamics for Unmanned Autonomous Vehicles*," IEEE Journal on Selected Areas in Communications (JSAC), and Special Issue on "*5G for Mission Critical Machine Communications*", IEEE Network Magazine.